AIChE

Nonisothermal Modeling of Heat Transfer Inside an Internal Batch Mixer

Yun Bai and Uttandaraman Sundararaj
Dept. of Chemical and Petroleum Engineering, University of Calgary, Calgary, Alberta, T2N 1N4, Canada

Krishnaswamy Nandakumar
Cain Dept. of Chemical Engineering, Louisiana State University, Baton Rouge, Louisiana, 70803

DOI 10.1002/aic.12484
Published online December 29, 2010 in Wiley Online Library (wileyonlinelibrary.com).

A nonisothermal transient process of temperature increase due to viscous heating was simulated for a 69 cm^3 internal batch mixer (BM) using a computational fluid dynamics (CFD) software, Polyflow 3.9 form ANSYS, Inc., to obtain the temporal temperature distribution and characterize the heat transfer between polymer melt and mixer wall. The melt temperature obtained from simulation was verified with experiments. Starting from a uniform temperature of 463 K, when a rotation speed of 5.24 rad/s is imposed, viscous heating caused a maximum temperature rise of 3 K for a polyethylene (PE) resin, and 6 K for a polystyrene (PS) resin. The transient flow fields inside the batch mixer were characterized with velocity profiles and a mixing index parameter, which show that laminar flow dominates inside the mixer while a small percentage of elongational flow, converging flow, and recirculation flow is also present. © 2010 American Institute of Chemical Engineers *AIChE J,* 57: 2657–2669, 2011
Keywords: batch mixer, nonisothermal, simulation, heat transfer, mixing, polymer processing

Introduction

The internal batch mixer is an important piece of polymer mixing equipment that is widely used in the rubber processing industry for producing final parts and in research laboratories for preliminary testing such as new materials development, studying polymer–polymer interactions and verifying mixing quality.[1–6] With the emergence of nanotechnology, internal batch mixers have also been used extensively to develop polymer nanocomposites and hybrids. This mixer is virtually in every polymer processing laboratory in universities and polymer companies that does product or process development. Since 1960, ThermoFisher Scientific alone has sold over one thousand of these mixers. Brabender has been selling these mixers for a longer time and has sold a similar number of these mixers. The mixer that is used to mix thermoplastic polymers and fillers consists of two roller blades counter-rotating in a mixing chamber. The mixing domain of the internal batch mixer can be divided into two parts (1) the narrow region between the rotor tip and chamber wall with unidirectional flow at high-temperature and high intensities of shear stress, and (2) the rest of the mixer with multidirectional flow at lower-temperature and lower intensities of shear stress.[7–8] The high viscosities of polymers and the large-shear rates generated in the narrow gap produce intensively high-shear stress to breakup polymer droplets or filler aggregates, and, therefore, promote polymer and/or filler dispersion. On the other side, the high viscosities of polymer, combined with high-shear rate, may also result in an increase in temperature due to viscous dissipation.[9–11] For a given polymer or filler, if the temperature rise due to viscous dissipation is significantly higher than the polymer's or filler's desired processing temperature, thermal degradation occurs and deteriorates the polymer properties. Moreover, in

Correspondence concerning this article should be addressed to U. Sundararaj at ut@ucalgary.ca.

reactive polymer compounding, a few degrees of temperature change can have significant effects on reaction rate, viscosity and other key parameters, and also in the resulting morphology.[12] The effect of viscous dissipation is also significant for mixing nanofillers with polymer, since for nanocomposites, compared to polymers or conventional composites, a significantly higher shear stress (produced by high-shear rate and high viscosity), and a relatively longer mixing time is required in order to get nanoscale dispersion that results in the desired material properties. As a result, temperature increase due to viscous dissipation is higher (duo to the combined effects of high-shear rate and high viscosity.) and materials' exposure time to higher-temperature is longer. Therefore, a better understanding of temperature rise due to viscous dissipation, together with shear rate distribution and flow patterns inside the internal mixer, would potentially provide useful information to evaluate mixing performance of this equipment and aid in development of new polymer materials in the mixer.

The approximate shear rate and shear stress in the unidirectional region of an internal batch mixer can be obtained from its rotor speed and torque.[13–19] By approximating the mixer as two concentric cylinder viscometers and using a Newtonian fluid, Goodrich et al.[13] calculated the viscosity, shear rate, and shear stress inside the mixer. For polyethylene and polystyrene, the calculated viscosity data are comparable with those obtained using an Instron capillary rheometer. Based on Goodrich's work, Bousmina et al.[17–18] developed more detailed correlations that derive the viscosity data from the torque rheometer for a non-Newtonian viscosity model. Although an average shear rate and shear stress in the unidirectional flow region can be obtained from these analytical models, the local flow information in that region is still missing and the shear rate and shear stress in the multidirectional flow region are unknown.

The flow field and mixing performance of an internal batch mixer have been studied by various researchers under isothermal and nonisothermal conditions.[19–27] Various viscous models have been used to characterize the non-Newtonian behavior of a polymer melt, but most of the work used 2-D geometry and the axial flow in the rotor axis directions was neglected. Nonisothermal 3-D modeling for a Banbury-type mixer was first studied by Kim and White[28] using the hydrodynamic lubrication theory and a rotating reference frame.

In this work, we study the transient process of the temperature development due to viscous dissipation inside an internal batch mixer using 3-D nonisothermal CFD modeling. Batch mixers are usually operated at a constant wall temperature well above the material's melting temperature. Once materials are added to the mixer, heat is transferred from the mixer wall to melt the material, and the temperature of the material increases. During this process, energy is supplied both from heaters inside the barrel and from the viscous heating generated from polymer melt due to rotating the rotors. After the temperature of material reaches the wall temperature, the melt temperature continues to increase due to heat generated inside the mixer by viscous dissipation until reaching a pseudo thermal steady state. At this point, energy is supplied by viscous heating to the melt and heat is transferred from the polymer melt to the mixer wall. When the pseudo thermal steady state is reached, the heat-transfer rate across the wall equals the power consumed. To keep the wall temperature constant, heat from the polymer melt needs to be removed from the mixer wall instantly. For any large-scale batch mixers used in industry, the mixer is cooled using cooling water or air, and the heat-transfer rate can be controlled by adjusting flow rate of the cooling fluid. However, because of the small volume of laboratory scale batch mixers, they are often cooled by surrounding air, and it is assumed that the heat removed by natural convection is sufficient to keep the wall temperature constant. In this article, we investigate the heat transfer during this viscous-heating-dominated process to verify whether a constant wall temperature can be maintained by natural air convection for a 69 cm^3 internal batch mixer.

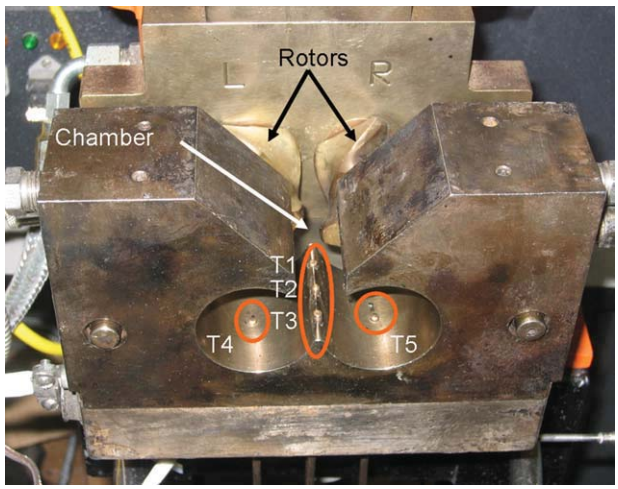

Figure 1. Experimental setup to record temperatures at five locations.

The protrusion of thermocouples into the mixer is: T1:0.5 mm; T2:1 mm; T3:1.5 mm; T4 and T5:0.2 mm, respectively. [Color figure can be viewed in the online issue, which is available at wileyonlinelibrary.com.]

In previous simulations of heat transfer in internal batch mixer, various simplified geometry and simplified conservation equations were used. For an accurate representation of the realistic scenario, a numerical model with full 3-D geometry and the complete mass, momentum and energy conservation equations are needed to capture the details of flow field and temperature development. The model results need to be compared with experimental data. In our work, the entire process was simulated using a commercial finite element code, Polyflow 3.9, for the full 3-D batch mixer geometry and the mesh superposition technique was used to handle the motion of the irregular counter-rotating elements.

Experiment

The Haake Rheocord 90 Torque Rheometer fitted with a Series 600 internal batch mixer was used for the experiment. The rollers and the experimental setup are shown in Figure 1. The barrel was preheated to a temperature of 463 K. The rotational speed of the left rotor (left side as seen from the front of the mixer) is 5.24 rad/s, and the speed of the right

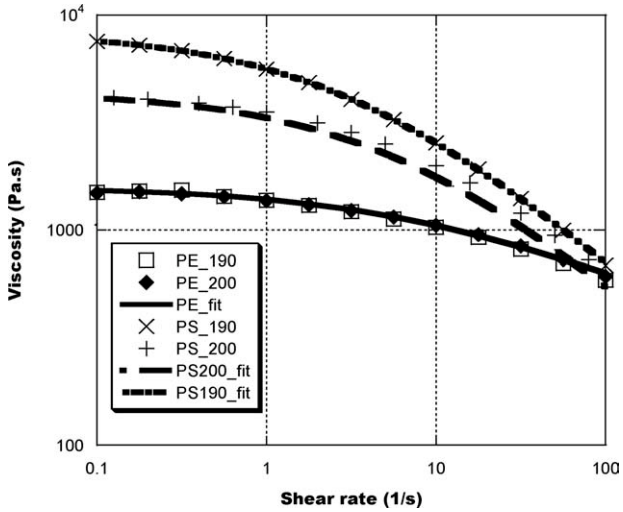

Figure 2. The viscosity data of PE and PS at 463 K (referred to as PE_190 and PS_190, respectively), and 473 K (referred to as PE_200 and PS_200, respectively).

The viscosity data was fitted by Carreau-Yasuda model. The fitted curves for PE at both 463 K and 473 K were overlapped and refereed as PE_fit. The fitted curves for PS at 463 K and 473 K were referred to as PS190_fit and as PS200_fit, respectively.

rotor is 2/3 of left rotor speed but in the opposite direction. Five thermocouples were inserted into the barrel of the mixing chamber to monitor the temperatures of polymer melt at different locations. Three of them ($T_{1,exp}$, $T_{2,exp}$, and $T_{3,exp}$) were located in the middle of the mixer between the two rotors, and were inserted into the polymer melt 0.5 mm, 1 mm and 1.5 mm from the wall, respectively. The other two ($T_{4,exp}$ and $T_{5,exp}$) were inserted into the left chamber and right chamber, respectively, and each protruded 0.2 mm into the mixer. All five thermocouples were type K with a diameter of 3.175 mm, and a response time of 0.6 s. The thermocouples were calibrated using a Fluke 725 calibrator, and the accuracy of the thermocouples is $\pm$ 0.1 K.

The polymer pellets were stuffed into the mixer until the mixer was fully filled. After the polymer pellets were completely melted, the melt temperature measured by thermocouples ($T_{1,exp}$ – $T_{5,exp}$) gradually increased until finally reaching constant values, which indicate that the previous described pseudo thermal steady state was reached. The motor was then stopped, and we waited until the melt temperatures slowly decreased to the barrel temperature. After the melt temperature was constant for 5 min, the motor was restarted. The melt temperature and the associated torque were recorded every second using an OPTO 22 data-acquisition system. During the restarting process, only viscous dissipation contributed to the polymer melt's temperature increase. The above process was repeated three times to check reproducibility.

High-density polyethylene (PE, Petromont, Canada), and polystyrene (PS, Dow Chemical) were used in the experiments. The rheological properties of PE and PS were measured using a Rheometrics RMS 800 rheometer with parallel-plate fixtures. The shear viscosities of PE and PS at 463 K and 473 K are shown in Figure 2.

Table 1. Properties of Polymer and Rotor

	Density at 473 K (kg/m^3)	Thermal capacity (J/kg·K)	Thermal conductivity (W/m·K)	Viscosity (Pa·s)
PE	740	2100	0.182	Eq.1
PS	882	2098	0.123	Eq.2
Rotor	8000	400	15	Not available

The combined Approximate Arrhenius law and Carreau-Yasuda law is used to characterize the viscosity change of PS vs. shear rate and temperature

$$\eta = 8357.8\left[1 + (0.3347\dot{\gamma})^{0.6686}\right]^{\frac{0.3215-1}{0.6686}} \cdot \exp(-0.006466(T - 463)) \quad (1)$$

The PE viscosity vs. shear rate curves at 463 K and 473 K are close to each other, so the viscosity dependence on temperature is neglected, and the viscosity dependence on shear rate is characterized by Carreau-Yasuda law

$$\eta = 1580\left[1 + (0.17\dot{\gamma})^{0.64}\right]^{\frac{0.7-1}{0.64}} \quad (2)$$

Other properties of PE and PS are summarized in Table 1. The rotor properties were assumed to be the same as those of the stainless steel AISI 316.

Computational Model

The following assumptions were made in the simulations:

1 The mixer is fully filled with polymer melt at all times.

2 The polymer melt is incompressible.

3 A no-slip boundary condition applies at the barrel wall and the rotors surfaces.

Gambit 1.3 was used to generate the geometry and the meshes of the internal batch mixer as shown in Figure 3. The mesh is composed primarily of tetrahedral mesh elements with a small amount of hexahedral, pyramidal, and wedge elements where appropriate. The average mesh size of the elements is about 0.8 mm with a larger size of 1 mm in the moving parts, and a smaller size of 0.1 mm in the gap areas.

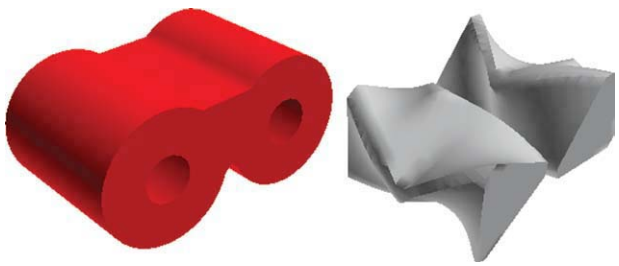

Figure 3. Geometry of the internal batch mixer and the roller blades.

[Color figure can be viewed in the online issue, which is available at wileyonlinelibrary.com.]

Table 2. Boundary Conditions Used in the Simulations

	Flow BC	Thermal BC
Left rotor	−5.24 rad/s	Not applicable
Right rotor	3.49 rad/s	Not applicable
Barrel wall	$V_n = 0$ $V_s = 0$	T = 463 K

*Counter-clockwise is positive.

The governing equations used in the simulation are the conservation laws for mass, momentum and energy. A mesh superposition technique (MST, Polyflow) was used to model internal moving rotors and the conservation equations are as follows:

Continuity equation

$$\nabla \cdot V = 0 \tag{3}$$

Momentum equation

$$H(V - \overline{V}) + (1 - H)\left(-\nabla p + \nabla \cdot \overline{\overline{\tau}} + \rho\left(\frac{\partial V}{\partial t} + V \cdot \nabla V\right)\right) = 0 \tag{4}$$

Energy equation

$$(1 - H)\left(\rho_f c_{pf}\left(\frac{\partial T}{\partial t} + V \cdot \nabla T\right) - \overline{\overline{\tau}} : \nabla V - \nabla \cdot (k_f \nabla T)\right) + H\left(\rho_s c_{ps}\frac{\partial T}{\partial t} - \nabla \cdot (k_s \nabla T)\right) = 0 \tag{5}$$

where the shear stress τ is related to the rate of strain tensor D through

$$\overline{\overline{\tau}} = 2\eta(\dot{\gamma}, T)\overline{\overline{D}} \tag{6}$$

and H is a step function, which is 0 for fluid field, and 1 for inner moving part. These equations were numerically solved using the finite element code, Polyflow 3.9 from Fluent, Inc. (now part of ANSYS, Inc.). The thermal boundary conditions (TBC), and flow boundary conditions (FBC) for the simulations are summarized in Table 2.

The simulations were performed on an IBM RS/6000 Power 4 workstation with 8 GB memory. It took an average of three weeks to complete each run.

Results and Discussion

Heat transfer

Heat Transfer Inside Mixer Due to Self-Heating. We studied the temperature evolution of polymer melt in an internal batch mixer at a constant wall temperature. The two roller blades counter-rotate with a specific rotation speed ratio of 3:2 (left rotor: right rotor). The left rotor's rotational speed is 5.24 rad/s, and the right rotor's rotational speed is 3.49 rad/s. So the left rotor rotates in a repeated cycle of 1.2 s, and the right rotor rotates in a repeated cycle of 1.8 s. The two rotors come back to their initial configuration every 3.6 s. The initial temperature of the polymer melt is the same as the wall temperature, and the temperature increases because of the heat generation caused by viscous dissipation. The energy balance can, therefore, be expressed in the following form

$$q_{st} = \frac{d(mc_pT)}{dt} = q_g - q_{out} \tag{7}$$

where q_{st} is the rate of change of stored energy in the melt which determines the temperature of the material, m is the amount of PS in the mixer, C_p is the heat capacity of *PS*, T is the temperature, q_g is rate of heat generation due to viscous dissipation, and q_{out} is the heat transfer from polymer melt to the mixer wall. The temperature of the polymer melt continues to increase until the heat transferred to the mixer wall equals the heat generated by viscous dissipation. A thermal steady state is then achieved. This steady state is periodically stable due to the rotors' configuration and rotational speed ratio. At 5.24 rad/s, the flow repeats every 3.6 s.

In the experiments, the torque evolution during the transient process was recorded for two cases; (a) PE melt, and (b) PS melt. The total mechanical power vs. time, plotted in Figure 4a and 4b, was obtained by multiplying the measured torque with the angular speed. The transient curves show that the power consumed jumps up from zero to its highest value when the rotors start rotating, and then gradually decreases to a constant value, which indicates that a thermal steady is reached.

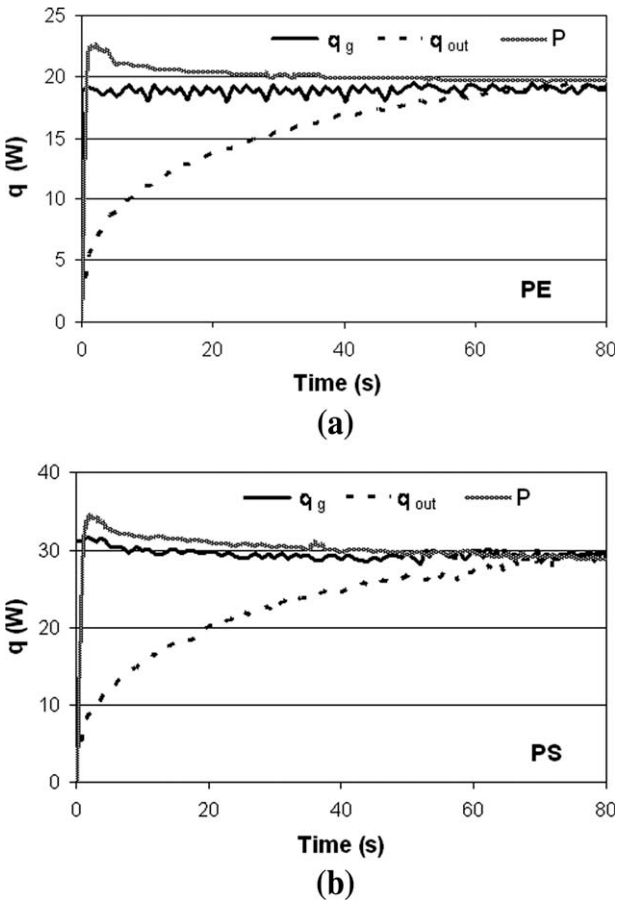

Figure 4. The evolution of q_g (rate of heat generation due to Viscous dissipation), q_{out} (heat transfer from polymer melt to the mixer wall), and P (experimentally measured power) for (a) PE, and (b) PS, respectively.

In the simulation, the heat generation rate $\boldsymbol{q}_g$ was calculated according to the following equation

$$q_g = \int_v tr(\sigma : D)dv \tag{8}$$

where σ is the Cauchy stress tensor, D is the rate of deformation tensor, $tr(\sigma: D)$ is the sum of the diagonal term of σ: D, V is the total volume of the mixer. The hear-transfer rate q_{out} is calculated as the magnitude of the heat flux integrated over the mixer wall

$$q_{out} = \iint_A \|-k\nabla T\|dA \tag{9}$$

where k is the heat conductivity of polymer melt, $\bigtriangledown T$ is the temperature gradient, and A is the total surface area of the mixer.

The evolution of q_g and q_{out} is plotted in Figure 4a for PE melt, and Figure 4b for PS melt. Although the mechanical power P should all be converted into heat q_g generated by viscous dissipation in the polymer melt, it is found that the experimentally measured P is initially higher than the theoretically calculated and then is slightly lower than q_g after thermal steady is reached. The explanation for the initial discrepancy is that part of mechanical energy is lost to overcome the frictional force in the bushings outside the mixer when the rotors start rotating. For mixers used in the rubber industry, it was reported that the mechanical loss in a large internal batch mixer is usually 10–15% of the total consumed energy depending on the size of the mixer.[29–30] In our case, the mechanical loss is much smaller because of the small size of the mixer (69 cm^3), and because a torque calibration that was done with an empty mixer. In addition, the current torque measurement may account for the small discrepancy at long times.

During the transient process, the heat generation by viscous dissipation raised the temperature of the material and, therefore, a temperature gradient was created between the polymer melt and the mixer wall. As temperature increases, the heat-transfer rate increases with time and finally equals the heat generation rate, as shown in Figure 4a and 4b. On the other hand, the temperature increase of the material resulted in a lower viscosity, and this in turn lowered the heat generation rate because the heat generation rate is proportional to material's viscosity according to Eq. 8. Because the viscosity of PE is less dependent on temperature than on the viscosity of PS, the rate of heat generated by viscous dissipation for PE does not change much over time, while the rate of heat generated by viscous dissipation for PS gradually decreases. For both materials, it takes about 80 s to reach steady state. The PS melt generally consumes more power than does the PE melt because of the higher viscosity of PS.

Heat transfer outside mixer due to self-heating

The heat-transfer rate from the simulation is plotted in Figure 4a for PE melt, and Figure 4b for PS melt. The corresponding overall heat-transfer coefficient can be calculated from the value of q_{out} using the following formula

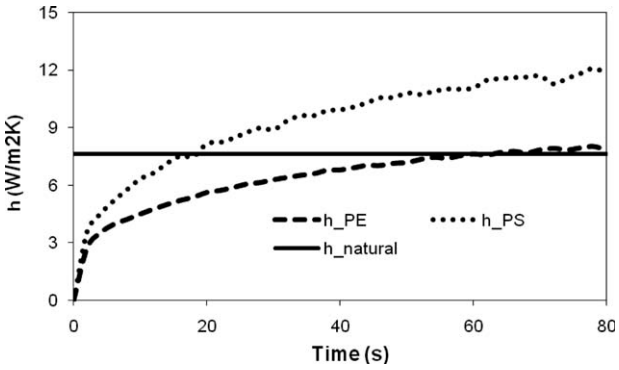

Figure 5. The evolution of the instantaneous overall heat-transfer coefficients (h_PE and h_PS) and the Churchill-Chu natural convection heat-transfer coefficient (h_natural) during the transient process.

$$h = \frac{q_{out}}{A_s(T_w - T_\infty)} \tag{10}$$

where A_s is the total outside barrel wall surface area, T_w is the constant wall temperature (463 K), and T_∞ is the surrounding room-temperature (ca. 298 K). If the instantaneous wall temperature is always constant, the temperature difference between the wall and the surrounding air would be constant. The overall heat-transfer coefficient would be proportional to the calculated heat-transfer rate and is shown in Figure 5 for both PE and PS. The h values increase over time for both materials.

In reality, the front and back walls of the mixer are vertical plates and have a much larger area than the side walls do. So the heat loss from the side walls can be neglected. For a steady free-convection flow over the vertical plates, the Churchill-Chu correlation equation[31] as follows can be used to calculate the overall natural convection heat-transfer coefficient

$$\overline{N}u = 0.68 + \frac{0.670Ra^{1/4}}{[1 + (0.492/\,\mathrm{Pr})^{9/16}]^{4/9}} \quad Ra \le 10^9 \tag{11}$$

The Nusselt number and the Rayleigh number are expressed as

$$\overline{N}u = \frac{\overline{h}_{Natural}L}{k} \tag{12}$$

$$Ra = \frac{g\beta(T_w - T_\infty)L^3}{v\alpha} \tag{13}$$

Based on the properties of air at the average temperature of 381 K (averaging T_w (463 K) and (298 K)), the Prandtl number is Pr = 0.6939, and the Rayleigh number is $Ra = 9.92 \times 10^6$ for this work. From this correlation, the natural convection heat-transfer coefficient was calculated to be 7.62 $W/m^2{\cdot}K$, and this value is shown in Figure 5. When the instantaneous overall heat-transfer coefficient is lower than $\overline{h}_{\text{Natural}}$, heat removed by the surrounding air is greater than the heat transferred from polymer melt and the heaters inside the wall work to keep the wall temperature constant. When the instantaneous

overall heat-transfer coefficient is higher than $\overline{h}_{\text{Natural}}$, the heat removed by the atmosphere is less than the heat transferred from polymer melt to the wall and will accumulate inside the wall to raise the wall temperature. As a result of wall temperature increase, less heat is transferred out from polymer melt and in turn the polymer melt temperature increases even faster. A high-polymer melt temperature can result in polymer degradation and other processing problems.

For the PE melt, the instantaneous heat-transfer coefficient to the wall is lower than the natural convection heat-transfer coefficient for the first 50 s and slightly higher afterwards. Because the surface area of the mixer and the temperature difference between the wall and the surrounding air (since we have constant wall temperature and constant surrounding air temperature), after thermal steady state is reached, the wall temperature can be kept constant via air convection only. For the PS melt, the instantaneous heat-transfer coefficient to the wall increases quickly and is greater than the calculated after about 20 s. The heat transferred from the PS melt cannot be completely removed by air convection and the PS melt temperature will be higher than it should be from the numerical simulation where a constant wall temperature was assumed. We also found that the experimental wall temperature was 1-2 K greater than the simulated temperature for the PS melt, while it matched the simulation result for the PE melt, i.e., it was constant with the h values of PE and PS vs. $\overline{h}_{\text{Natural.}}$

The time-averaged heat-transfer coefficient from the simulation is found using

$$\overline{h} = \frac{\sum_{n=1}^{N} \overline{h}(t) \cdot \Delta t}{N \cdot t} \tag{14}$$

where Δt is the time step, and N is the number of time steps. On the first 80 s, the time average heat-transfer coefficient is 6.3 W/m^2·K for PE and 9.2 W/m^2·K for PS. These values are close to the natural convection heat-transfer coefficient determined from the Churchill-Chu correlations, so this indicates that air convection can remove most of the heat generated in the polymer melt due to viscous heating. However, it should be noted that correlations like the Churchill-Chu relation have ±25% error.

Temperature evolution

Three thermocouples designated as $T_{1,exp}$, $T_{2,exp}$, $T_{3,exp}$ are located in the middle ridge of the mixer as shown in Figure 1. The melt temperature at the three middle locations vs. time for the experiment and the simulation are shown in Figure 6a for PE melt, and Figure 6b for PS melt. The predicted temperatures are taken from the simulation results at the same locations and are designated as $T_{1,sim}$, $T_{2,sim}$, $T_{3,sim}$. To understand the temperature gradient close to the wall, the thermocouples protrude into the mixer at different depths. For both polymers, it takes about the same time for the three temperatures to reach their corresponding thermal steady-state temperatures. The time for the temperature to reach thermal steady state from the simulation also matches well with the time obtained from the experiment. All temperatures initially increase with time until the thermal steady state is achieved. The experimentally measured $T_{2,exp}$ and

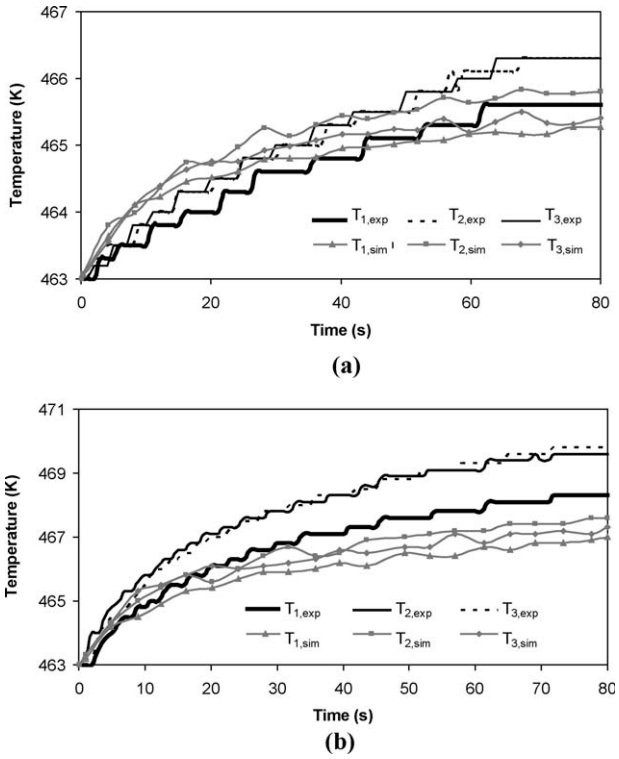

Figure 6. Comparisons of the experimentally measured point temperatures at three different locations (T1, T2 and T3, respectively) with those predicted from the simulations for (a) PE, and (b) PS.

$T_{3,exp}$ match each other in the first 80 s, while the experimentally measured $T_{1,exp}$ is always lower than $T_{2,exp}$ and $T_{3,exp}$. Since the temperature of polymer melt inside the mixer is always higher than the preset wall temperature in our work, the measured temperatures at locations closer to the wall are lower than the temperature away from wall even though this may not represent the actual melt temperature. The actual melt temperature at locations near the walls is higher than the measured values due to the interface of the controlled constant barrel temperature which will lower the temperature measured. Even though $T_{3,exp}$ has a 0.5 mm deeper protrusion into the melt than $T_{2,exp}$, the recorded temperatures are about the same because $T_{3,exp}$ is closer to the front wall while $T_{2,exp}$ is in the middle of the mixer where it should be hotter. $T_{1,exp}$ is close to the back wall and has the less protrusion into the melt, so the recorded temperature $T_{1,exp}$ is much lower than the other two. Experimentally, viscous heating causes about a 3 K increase for the PE melt, and a 6 K increase for the PS melt at all three locations.

The temperatures predicted from the simulation at the same three locations have curves similar to the measured data except that in the simulation result, $T_{2,sim}$ is slightly higher than $T_{3,sim}$. The difference between the experimental data and the predicted data is due to the fact that the wall temperature is constant throughout the process in the simulation, while in the experiment, the wall temperature fluctuates around the preset temperature because of the competing effect

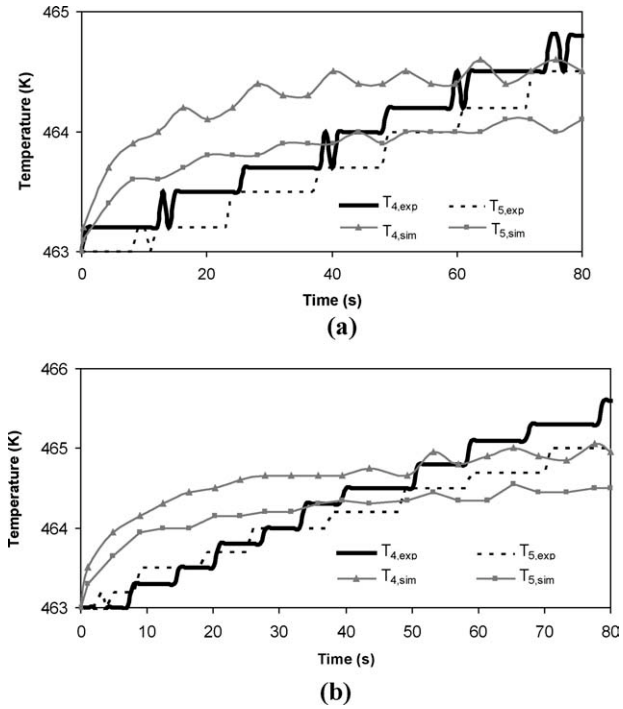

Figure 7. The temperature development of thermocouple T4 and T5, located in the left chamber and the right chamber, respectively, for (a) PE, and (b) PS.

of heat removal by natural air convection and the barrel heating system. Because of inefficient heat removal by natural air convection, experimental barrel temperature may exceed the simulated temperature. This is especially true for the PS case (Figure 6b); because the heat-transfer coefficient in the melt is greater than the heat-transfer coefficient due to natural convection outside the mixer (see Figure 5). In addition, the measured temperatures at the locations closer to the front and back walls have a larger deviation from the simulated value.

While the wall temperature of the mixer in the simulation can be fixed at a constant value, the wall temperature of the mixer in reality is controlled by a dynamic system. For all internal batch mixers, the mixer walls have a built-in heating system to supply heat. Although larger internal batch mixers also have a controlled cooling system to remove heat either by forced air or water cooling, the mixer used in our experiments is cooled by the surrounding air only. During a heating process, the heating system inside the wall not only supplies heat to the material inside the mixer, but also provides heat to the surrounding air because the operating temperature is always much higher than room-temperature. During the cooling process, the heat transferred from the material to the wall is removed by the air surrounding the mixer and the actual wall temperature tends to be slightly higher than the preset wall temperature, which results in the slightly higher overall rate of heat transfer from the mixer to surrounding air.

Thermocouple $T_{4,exp}$ and $T_{5,exp}$ are located at the bottom of the left chamber and the right chamber, respectively. Because of the small clearance between the tips of the rotors and the wall, $T_{4,exp}$ and $T_{5,exp}$ are only inserted into polymer melt about 0.2 mm. Figure 7 shows the comparisons of the experimentally measured temperatures with predicted ones from simulation ($T_{4,sim}$ and $T_{5,sim}$). Close to the mixer wall, the temperatures measured by these two thermocouples are much lower than the other three in the middle. In our work, the left rotor of the mixer runs 50% faster than the right one. So the temperature next to the left rotor will be greater than that near the right rotor. For the same clearance between the rotors and the wall, higher rotational speed (i.e., rotor tip velocity) means a higher shear rate and more viscous heating. Therefore, at longer times, the average temperature in the left chamber is always higher than the average temperature in the right chamber. Using the same reasoning that was used for $T_{1,exp}$, $T_{2,exp}$ and $T_{3,exp}$, we can explain why the measured values at $T_{4,exp}$ and $T_{5,exp}$ are also higher than the predicted ones. At shorter times, because the thermocouples at the left and right chamber are located so close to the barrel wall, the controlled barrel wall temperature may interfere with the actual measurement of the melt temperature. Essentially, when we have a lower-temperature difference (i.e., at shorter time), the experimentally measured temperatures will be lower than the actual melt temperature. Overall the temperature at $T_{4,exp}$ increases 1.8 K for PE and 2.5 K for PS, while at $T_{5,exp}$ increases 1 K for PE and 1.5 K for PS. Again, the high viscosity of PS creates higher viscous dissipation and a higher temperature increase as shown in Figure 7b.

Figure 8 shows the averaged temperature obtained from simulations along the axial direction at different times for PE and PS (i.e., the surface-averaged temperature was obtained by integrating the point temperatures of the melt over the cross-sectional surface and dividing it by the cross-sectional area.) The axial distance was normalized as the axial distance divided by the mixer length giving a range from 0 to 1. Initially, the temperature in the flow domain is very close to the starting temperature and the average temperature profile is quite flat. Due to the heat generated by viscous dissipation, the temperature increases and a symmetric temperature profile is developed. The middle cross-section surface (i.e., $z = 0.5$) has the highest temperature at any time. The curves of average temperature vs. axial distance increase or decrease sharply at locations close to the back and front walls, respectively, and become flat around the middle of the mixer. Because of its higher viscosity, thus, its higher viscous dissipation, the PS melt has a higher average temperature than the PE melt over the whole transient process.

Additional Simulation Results

More detailed information about the temperature field and the flow field can be obtained from the simulation results to give us a better understanding of what happens inside the mixer during the simulated transient process.

Heat flux

Figure 9 shows the heat flux at the mixer wall as a function of circumferential distance at three different times for PE and PS, respectively. The heat flux q'' is calculated by the following equation

$$q'' = \|-k\nabla T_{T=T_w}\| \tag{15}$$

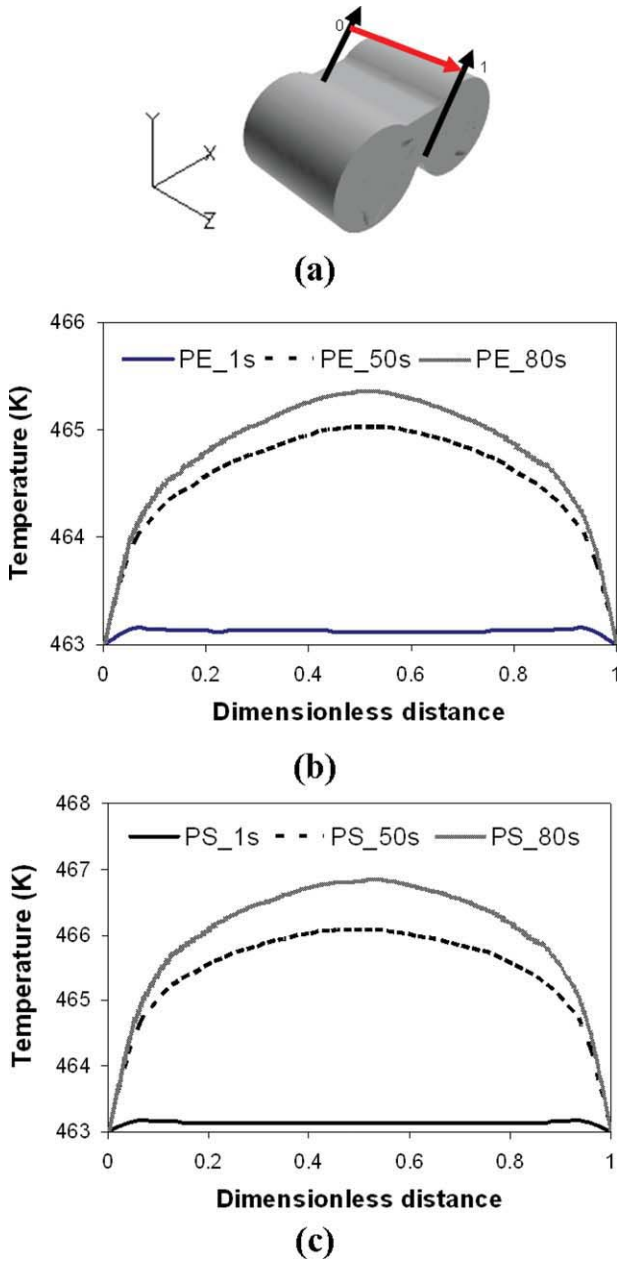

Figure 8. Surface-averaged temperature changes along the axial distance of the entire mixer: (a) illustration of the normalized axial distance, (b) temperature change for PE, and (c) temperature change for PS.

The origin (x, y, z) is (0, 0, 0). Note different scales on (b) and (c). [Color figure can be viewed in the online issue, which is available at wileyonlinelibrary.com.]

The heat flux direction is perpendicular to the wall and flows out of the mixer as indicated by the black arrows. The starting point in the plot is shown as a dot on the top of the mixer in Figure 9a, and the heat flux is plotted in the direction indicated by the white arrow tangent to the circumference from the right chamber to the left chamber and back. For both materials, the heat flux across the wall increases with time and finally reaches a thermal steady state. From 50 s to 80 s, the heat flux increases very little, although the temperature of the polymer melt continues to increase and reaches a thermal steady state as shown in Figure 6. At the thermal steady state, the average heat flux for PE is approximately 700 W/m^2 in the right chamber, and 1050 W/m^2 in the left chamber. For PS, the average heat flux is approximately 900 W/m^2 in the right chamber, and 1300 W/m^2 in the left chamber. The heat flux ratio of the right chamber versus left chamber is about 2/3: the same as the rotation speed ratio of the right rotor vs. left rotor.

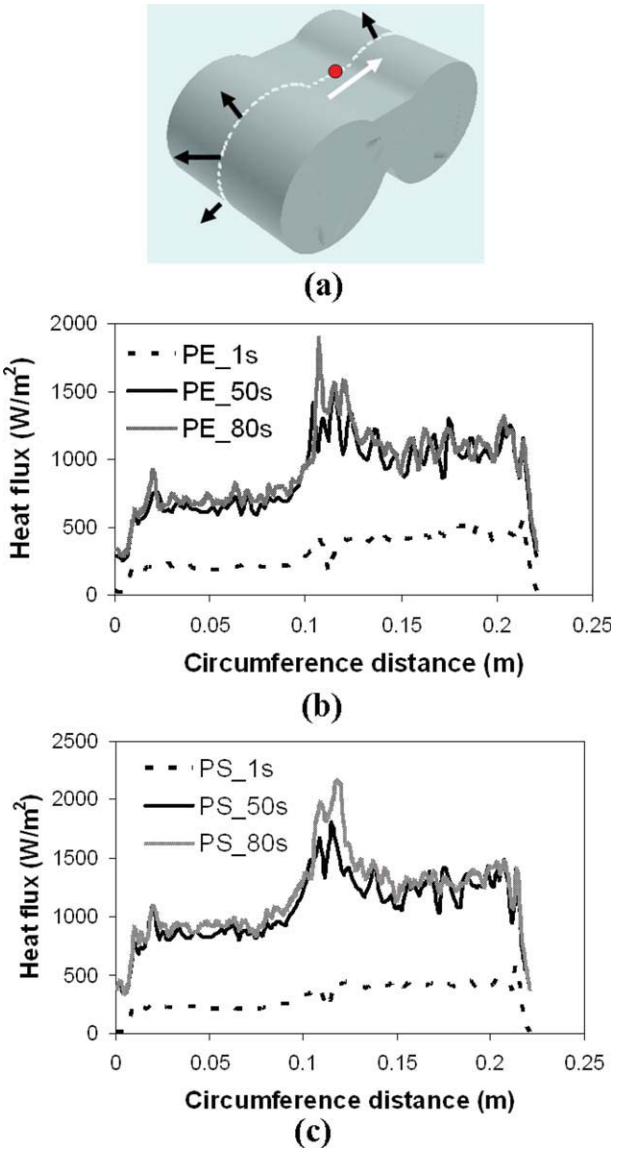

Figure 9. Heat flux across wall around the circumference at the mid-depth for different times (a) location where the heat flux is calculated, (b) heat flux for PE, and (c) heat flux for PS.

[Color figure can be viewed in the online issue, which is available at wileyonlinelibrary.com.]

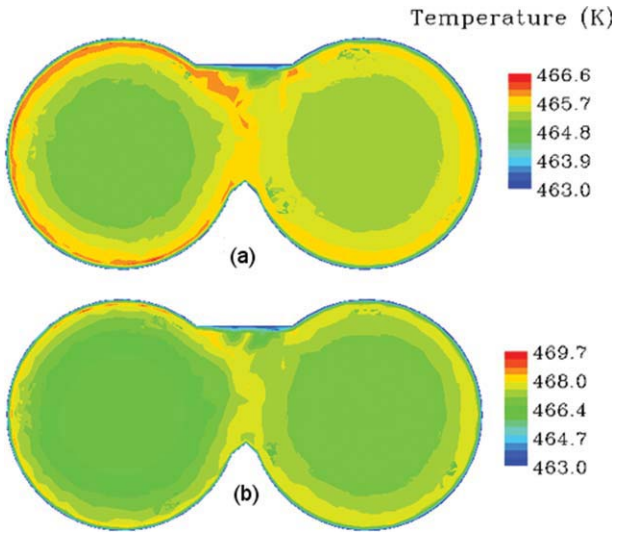

Figure 10. The steady-state temperature distribution at the axial middle cross section (a) PE, and (b) PS.

[Color figure can be viewed in the online issue, which is available at wileyonlinelibrary.com.]

Temperature distribution at a cross section

Figure 10 shows the steady-state temperature distribution at the axial middle cross section for both PE and PS from a starting temperature at 463 K. Because of a higher rate of viscous heating near the wall, the temperature at the clearances is as high as 466.6 K for PE and 469.7 K for PS, while the average temperature in the mixer increases to 464.5 K for PE and 465.5 K for PS. It is found that the temperature in the clearance area is about 1 K higher than the temperature in the area between two rotors, and that the temperature in the left rotor side is about 0.5–1 K higher than the temperature in the right side. Considering the size of the mixer is only 69 cm^3, the temperature rise is relatively large for both polymers.

Velocity profile

Due to the high viscosities of polymer melts, laminar flow is the dominant flow in polymer mixing equipment. Various laminar flow patterns such as shearing, squeezing or elongational flows play a very important role in achieving uniformity of polymer blends and nanocomposites, and in dispersing minor components throughout the matrix.[32] As shown in Figure 11, the velocity profiles are very similar for PE and PS. The velocity profile consists of two parts: high-shear flow in the region between rotor tips and wall; and elongational flow in the middle region between the two rotors and in the converging-diverging sections as the gap between rotors and wall changes. When viewing the velocity profiles in Figure 11, one should note that the rotational speed ratio of the left rotor to the right rotor is 3 to 2 in the internal batch mixer; the magnitude of the velocity is scaled by the arrow length; and the color on the legend bar also indicates the magnitude of the velocity vector. The maximum velocity of 0.1 m/s occurs on the tip of the left rotor where the gap is the smallest. While a small amount of extensional flow exists in the middle area between two rotors, shear flow dominates in the narrow region between the rotor tip and chamber wall. As expected, the largest velocity always occurs near the rotor tips and, therefore, the polymer melt is squeezed in these areas. In the gaps between the two rotors, the materials from left and right chambers meet in the upper area and then split again in the lower part. The velocity profiles show that shear flow dominates in the gap between the rotors and barrel wall, and all other flow types such as folding, elongation and splitting occur mainly in the middle region between the two rotors.

The flow types were further characterized using a mixing index (MI) parameter defined by Manas-Zloczower,[33] which was also called flow strength or flow number to quantify the dispersion

$$MI = \frac{|D|}{|D| + |\omega|} \tag{16}$$

where $|D|$ and $|\omega|$ were the magnitudes of the rate of strain and vorticity tensors, respectively. MI was the relative portion of the magnitude of the rate of strain vs. the sum of the magnitude of the rate of strain and the magnitude of the vorticity tensor. For pure solid rotation, the magnitude of the rate of strain was zero because there was no strain change and, therefore, MI was zero. For shear flow, the magnitude of the rate of strain equaled the magnitude of the vorticity tensor, and MI equaled 0.5. The magnitude of the vorticity tensor was zero for elongational flow and MI equaled 1. Since MI was an indicator of flow type, it became an indirect parameter to characterize dispersive mixing. This parameter was used by Manas-Zloczower group[34–35] to compare the dispersive mixing efficiency of different mixing equipment and processing conditions.

Figure 12 showed MI distributions of BM at a cross section. The blue, green and red color indicated solid rotation (0), shear flow (0.5), and elongational flow (1), respectively. It can be seen that the rotors experienced the pure rotation all the time. Elongational flow existed in the middle part between the two rotors while shear flow dominated in the rest of the chamber.

Since the two rotors have different configurations along the axial direction, the velocity profiles at different

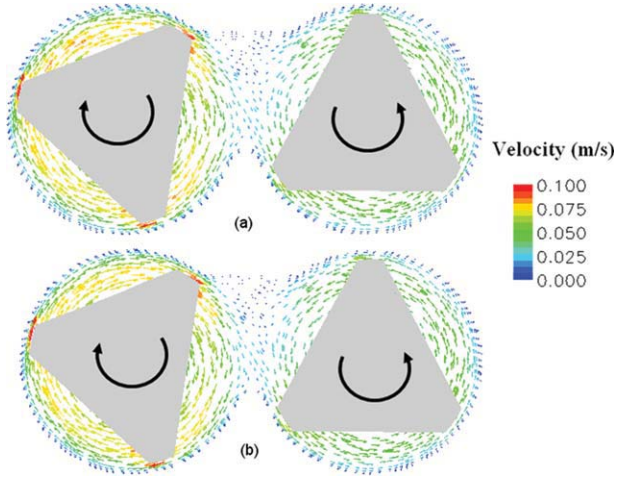

Figure 11. Steady-state velocity profiles at the axial middle cross section for (a) PE, and (b) PS.

[Color figure can be viewed in the online issue, which is available at wileyonlinelibrary.com.]

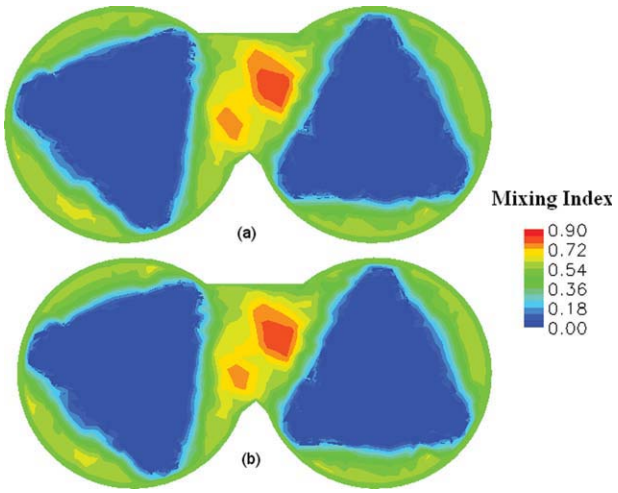

Figure 12. Mixing index (MI) distribution at the axial middle cross section (a) PE, and (b) PS.

MI is 0 for pure rotational flow, 0.5 for shear flow and 1 for elongational flow. [Color figure can be viewed in the online issue, which is available at wileyonlinelibrary.com.]

axial cross sections are different. Figure 13a,–c plot velocities at the center portion of three axial cross sections at the dimensionless axial distances 0.36, 0.50, and 0.86. Figure 13a shows the section at $z = 0.36$, which is near the back of the mixer. The tip of the right rotor is slightly higher than that of the left rotor, and, hence, the flow from the right chamber is folded and then joins the flow from the left. Since the left rotor tip pushes the materials into the right chamber, most of the materials in the gap in the middle of the mixer go to the right chamber. In Figure 13b at $z = 0.5$, the flow pattern is in the opposite direction, but the extent of folding of the flow from the left chamber at this location is less than that from the right rotor at $z = 0.36$. When the tips of the two rotors are at the same level as in Figure 13c ($z = 0.86$), the flows from the two chambers join together and then split almost equally in two directions. There is not much folding in this configuration.

Figure 14a–f shows how the flow field changes between two rotors for the cross section at $z = 0.50$ during one rotation of the left rotor ($\theta = 0^\circ$ to $\theta = 360^\circ$), which takes 1.2 s at 5.24 rad/s. Due to the different rotational speeds of the two rotors, different configurations occur creating various flow patterns that promote the dispersion and distribution of the minor component. Depending on the positions of the two tips, folding may occur in the upper, center, and/or bottom parts of the middle section of the mixer, or no folding may occur at all. Initially in Figure 14a, the materials mix and mostly flow into the right chamber and folding is seen near the bottom of the mixer. After the left rotor turns 60° (Figure 14b), the tips of two rotors are almost in the same position and there is no folding at all. At 120° (Figure 14c), the tips of both rotors are located in the central area with the right rotor located slightly higher. Hence, the materials are squeezed and elongated to the maximum extent. In the next two positions (Figure 14d and e), the flow is folded near the bottom of the mixer and in each case material flows to the chamber opposite to the tip that is located in a lower

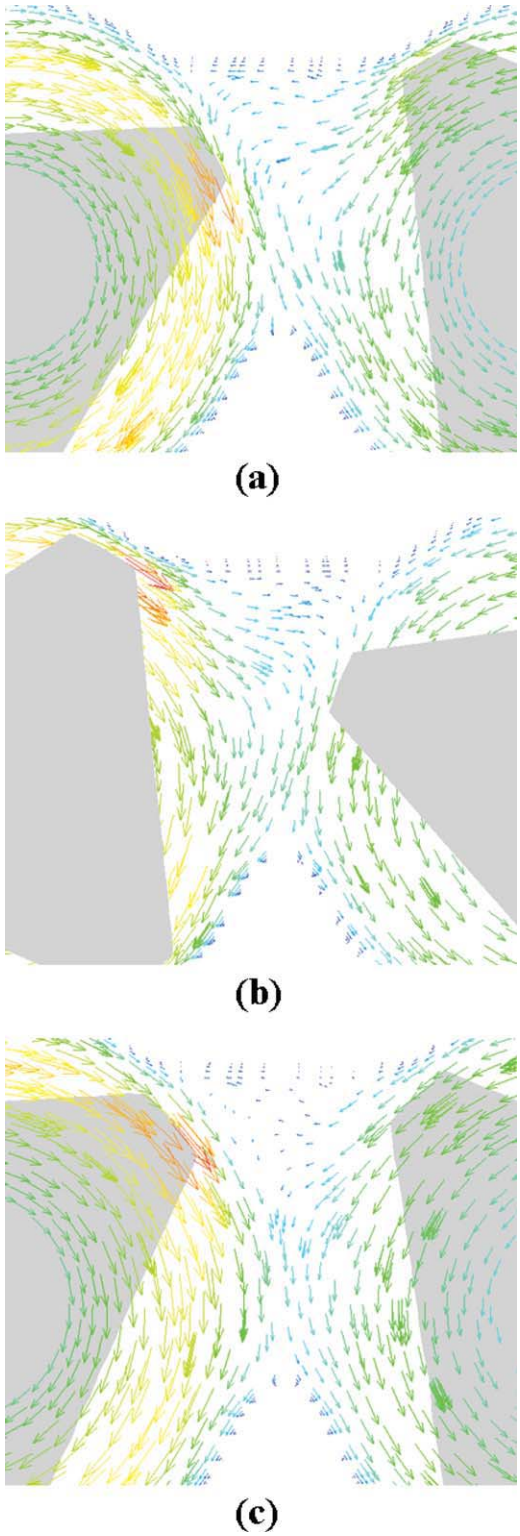

Figure 13. The radial velocity profiles at three typical cross-sections (scaled by the same legend bar shown in Figure 11.), (a) the enlarged center of $z = 0.36$, (b) the enlarged center of $z = 0.50$, and (c) the enlarged center of $z = 0.86$.

[Color figure can be viewed in the online issue, which is available at wileyonlinelibrary.com.]

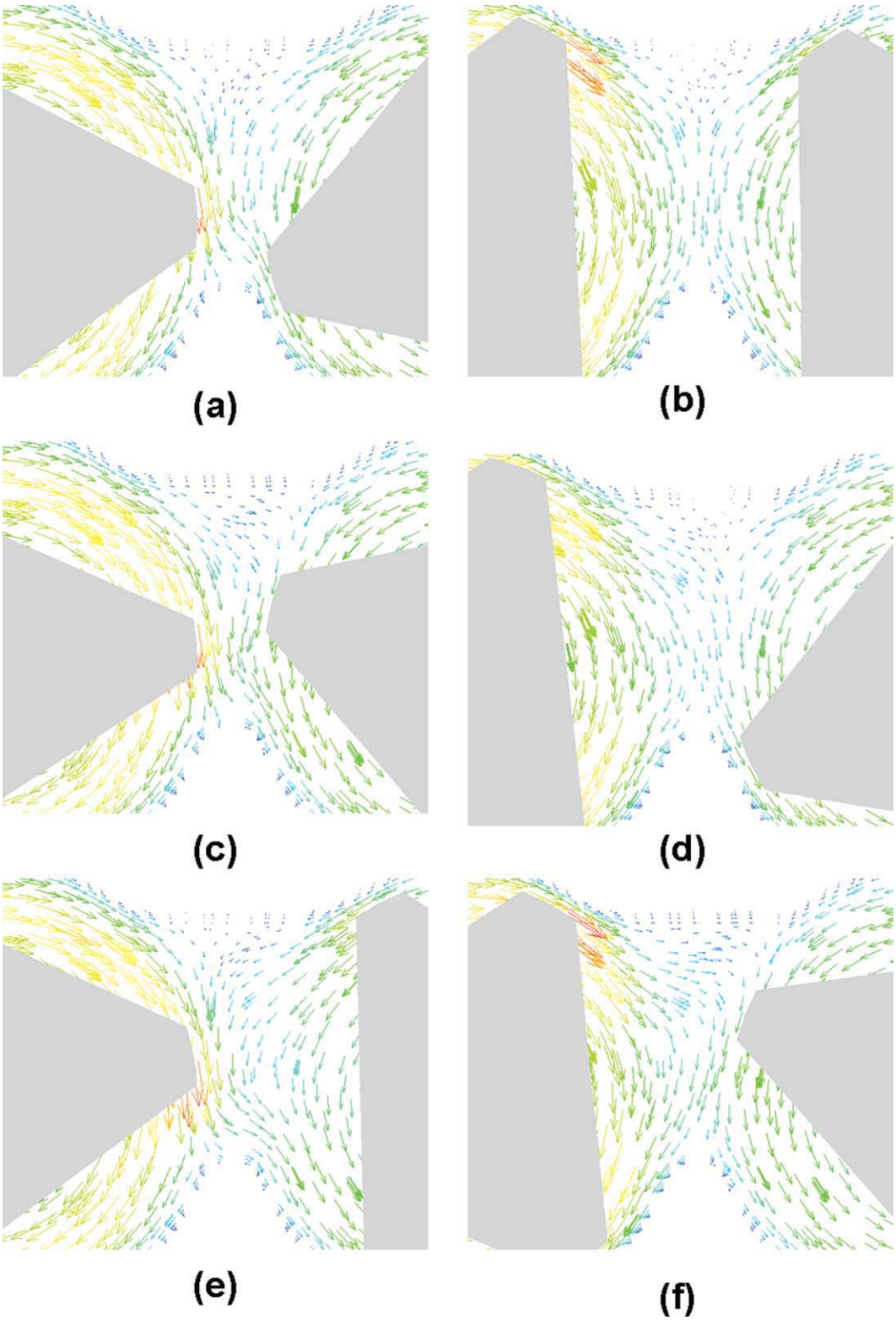

Figure 14. Transient velocity profiles of the internal batch mixer at cross section $z = 0.50$ (scaled by the same legend shown in Figure 11).

a–f shows velocity change at the center of MB during one turn of the left rotor (a) $\theta = 0$, (b) $\theta = 60°$, (c) $\theta = 120°$, (d) $\theta = 180°$, (e) $\theta = 240°$, and (f) $\theta = 300°$. [Color figure can be viewed in the online issue, which is available at wileyonlinelibrary.com.]

position. When left rotor turns 300° (Figure 14f), both tips appear in the upper part of the mixer and the folding occurs mainly near the top of the mixer. Although the repeating period is 3.6 s at a rotational speed of 5.24 rad/s, the positions of the tips of both rotors in each particular cross section return to their original locations every 1.2 s because there are three identical tips per rotor.

Conclusion

For both the PE and the PS melt, the mechanical power consumed was calculated from the experimental torque and matched with the value obtained from a 3-D CFD simulation. The predicted heat-transfer coefficient h from simulation increases with time, and is in rough agreement with h values obtained experimentally. The observed wall temperature is about 1-2 K higher than the preset value of 463 K. Because of the increase in wall temperature that occurs in the experiment, the temperature of the PS melt is higher than the predicted value. Natural air convection is sufficient to keep the mixer wall temperature constant for the low-viscosity materials, but for high-viscosity materials (i.e., having higher viscous dissipation), forced air convection is necessary to remove the heat produced by viscous heating so that a constant wall temperature can be maintained.

Simulation results give us a detailed picture of the temperature distribution and flow distribution inside the mixers and how these distributions develop over time. The higher rotational speed of the left rotor results in a higher temperature and higher heat flux in the left chamber. The simulation results also verified that multiple flow modes coexist in the mixer. For both PE and PS, experiments and simulation showed that it takes approximately 80 s to reach a thermal steady state for a left rotor rotational speed of 5.24 rad/s. The maximum temperature rise due to viscous dissipation is about 3 K for PE and 6 K for PS.

The methodology developed in this work can be further used to model larger-scale mixers, where the temperature variation due to viscous dissipation is much more significant, but experimental measurements are limited.

Notation

A = local surface area
C_p = thermal capacity
$\overline{\overline{D}}$ = rate of deformation tensor
g = gravity
h = heat-transfer coefficient
$\overline{h}$ = time-averaged mean heat-transfer coefficient
k = thermal conductivity
L = characteristic length
m = mass
$\overline{Nu}$ = mean Nusselt number
P = pressure
Pr = Prandtl number
q'' = local heat flux
Re = Reynolds number
t = time
Δt = time interval
T = temperature
T_m = measured temperature or melting temperature
V = velocity vector or Volume

Greek letters

α = thermal diffusivity
$\dot{\gamma}$ = shear rate
η = viscosity
η_0 = zero shear rate viscosity
ρ = density
$\overline{\overline{\tau}}_{,\tau}$ = stress tensor

Literature Cited

1. Bousimina M, Ait-Kadi A, Faisant JB. Determination of shear rate and viscosity from batch mixer data. *J Rheology*. 1999;43(2):415–433.
2. Yamaguchi M, Wagner MH. Impact of processing history on rheological properties for branched polypropylene. *Polymer*. 2006;47(10):3629–3635.
3. Campanelli JR, Gurer C, Rose TL, Varner JE. Dispersion, temperature and torque models for an internal mixer. *Polym Eng Sci*. 2004;44(7):1247–1257.
4. Yamaguchi M, Todd DB, Gogos CG. Rheological properties of LDPE processed by conventional processing machines. *Adv Polym Technol*. 2003;22(3):179–187.
5. Sundararaj U, Macosko CW. Drop breakup and coalescence in polymer blends: The effects of concentration and compatibilization. *Macromolecules*, 1995;28(8):2647–2657.
6. Manas-Zloczower I. Studies of mixing efficiency in batch and continuous mixers. *Rubber Chem Technol*. 1994;67(3):504–528.
7. Palmgren H. Processing conditions in the batch-operated internal mixer. *Rubber Chem Technol*. 1974;48:462–494.
8. Li H, Hu GH. A two-zone melting model for polymer blends in a batch mixer. *Polym Eng Sci*. 2001;41(5):763–770.
9. Soltani S, Sourki FA. Effect of carbon black type on viscous heating, heat build-up, and relaxation behavior of SBR compounds. *Iran Polym J*. 2005;14(8):745–751.
10. Herrera-Velarde JR, Zenit R, Mena B. Measurement of the temperature rise in non-Newtonian oscillatory pipe flows. *J Non-Newtonian Fluid Mech*. 2003;109:157–176.
11. Wei DW, Luo HB. Finite element solutions of heat transfer in molten polymer flow in tubes with viscous dissipation. *Int J Heat Mass Transfer*. 2003;46:3097–3108.
12. Hu GH. Modeling reactive blending: an experimental approach. *J Polym Sci: Part B: Polym Phys*. 1998;36:2153–2163.
13. Goodrich JE, Porter RS. A rheological interpretation of torque-rheometer data. *Polym Eng Sci*. 1967;7(1):45–51.
14. Blyler LL, Daane JH. An analysis of Brabender torque rheometer data. *Polym Eng Sci*. 1967;7(3):178–181.
15. Marquez A, Quijano J, Gaulin M. A calibration technique to evaluate the power-law parameters of polymer melts using a torque-rheometer. *Polym Eng Sci*. 1996;36(20):2556–2563.
16. Mallette JG, Soberanis RR. Evaluation of rheological properties of nonnewtonian fluids in internal mixers: An alternative method based on the power law model. *Polym Eng Sci*. 1998;38(9):1436–1442.
17. Bousmina M, Ait-Kadi A. Faisant JB. Determination of shear rate and viscosity from batch mixer data. *J Rheology*. 1999;43(2):415–433.
18. Ait-Kadi A, Marchal P, Choplin L, Chrissemant A, Bousmina M. Quantitative analysis of mixer-type rheometers using the coquette analogy. *Can J Chem Eng*. 2002;80:1166–1174.
19. Clarke J, Petera J. Modeling dispersive mixing of rubber compounds. *Rubber Chem Technol*. 1999;72(5):807–828.
20. Hutchinson BC, Rios AC, Osswald TA. Modeling the distributive mixing in an internal batch mixer. *Int Polym Process*. 1999;14(4):315–321.
21. Nassehi V, Ghoreishy MHR. Finite element analysis of mixing in partially filled twin blade internal mixers. *Int Polym Process*. 1998;13(3):231–238.
22. Ghoreishy MHR; Nassehi V. Modeling the transient flow of rubber compounds in the dispersive section of an internal mixer with slip-stick boundary conditions. *Adv Polym Technol*. 1997;16(1):45–68.
23. Valera TS, Demarquette NR, Toffoli SM. Effect of filling factor on the determination of shear rate and viscosity from batch mixer. *J Polym Eng*. 2004;24 (4):409–433.
24. Jongen T. Characterization of batch mixers using numerical flow simulations. *AIChE J*. 2000;46:2140–2150.

25. Gramann PJ, Mätzig J.C, Osswald TA. Simulating the non-isothermal mixing of polymer blend using the boundary element method. *J Reinf Plas Compos*. 1993;12:787–799.
26. Malkin AY, Baranov AV, Dakhin OK. Non-isothermal dispersive flow of a rubber mixture inside an internal rotor mixer. *Int Polym Process*. 1995;10(2):99–104.
27. Nassehi V, Salemi R. Finite-element modeling of non-isothermal viscometric flows in rubber mixing. *Int Polym Process*. 1994;9(3):199–204.
28. Kim JK, White J L. Non-newtonian and nonisothermal modeling of 3D-flow in an internal mixer. *Int Polym Process*. 1991;6(2):103–110.
29. Palmgren H. Processing conditions in the batch operated internal mixer. *Rubber Chem Technol*. 1975;48:462–494.
30. Nakajima N. Mechanism of mixing in internal mixer and energy-based modeling. *Polym Int*. 1996;41:23–33.
31. Churchill SW, and Chu HHS. Correlating equations for laminar and turbulent free convection from a vertical plate. *Int J Heat Mass Transfer*. 1975;18:1323–1329.
32. Gogos CG, Tadmor Z, Kalyson DM, Hold P. Polymer processing: an overview. *Chem Eng Prog*. 1987;6:33–58.
33. Manas-Zloczower I. Analysis of mixing in polymer processing equipment. *Rheol Bullet*. 1997;66(1):5–8.
34. Yang HH, Manas-Zloczower I. 3-D flow field analysis of a Banbury mixer. *Int Polym Process*. 1992;7(2):195–203.
35. Li T, Manas-Zloczower I. Flow field analysis of an intermeshing counter-rotating twin screw extruder. *Polym Eng Sci*. 1994;34:551–558.

Manuscript received July 29, 2010, and revision received Oct. 15, 2010.